

Popping: A granular transition

A. Ghosh¹, M. M. Bandi^{2,*} and S. Ghosh^{1,†}

¹Department of Condensed Matter Physics and Materials Science, Tata Institute of Fundamental Research, Mumbai 400005, India

²Nonlinear and Non-equilibrium Physics Unit, OIST Graduate University, 1919-1 Tancha, Onna-son, Okinawa 904-0495, Japan



(Received 20 January 2024; accepted 12 August 2024; published 6 September 2024)

In experiments conducted on a weakly confined 2D assembly of deformable cylinders subjected to rapid in-plane shear loading, we have identified the key obstacle in achieving compaction. This obstacle involves a dynamic transition between mechanical instabilities, progressing from in-plane rearrangement to out-of-plane popping as the density increases. The popping effect reinforces the frictional constraints from the confining wall and restricts particle mobility, impeding the system from attaining greater compaction. We quantify this transition and demonstrate that interparticle friction contributes to smoothing the transition.

DOI: [10.1103/PhysRevResearch.6.033255](https://doi.org/10.1103/PhysRevResearch.6.033255)

I. INTRODUCTION

Achieving a desired level of granular compaction, a problem with both practical [1–4] and scientific significance [5,6], can be attained either through static and dynamic compaction [1,7–9] or by supplying energy via small-amplitude vibrations [5,10–14]. The former involves plastic deformation of the granular media [15,16] while the latter achieves compaction by mobilizing particles [11]. Therefore, reduced particle mobility can significantly hinder the compaction process [14]. In this study, we demonstrate how frictional constraints triggered by mechanical instabilities, can restrict the compaction process. Lowering mobility through frictional constraints is broadly applicable in soft systems; consider two deformable spheres confined within a slightly undersized cylindrical container. With small compression, they bounce back upon release; however, under greater force, they deform sideways, transferring their elastic force to the walls and becoming immobilized.

In this article, we experimentally study the compaction of a 2D assembly of deformable granular cylinders under repetitive shear loading. Our setup involves weak confinement, with a small gap between the granular material and its top confining plate. This type of weak confinement is commonly used in experimental setups aimed at studying the mechanical properties of 2D granular packings [17]. It is worth noting that experiments without a top confining plate operate under loads where out-of-plane buckling instability can be prevented [18,19]. The grains move in response to an applied stress and their motion is resisted by the formation of load-bearing force

chains. In cases where space allows, these chains can buckle within the plane due to increased stress, leading to particle rearrangement and elastic deformation of the soft grains. Upon stress removal, the stored elastic energy is released, relaxing the compact state. This happens at lower densities. At higher densities, some of the particles wedge out of the plane under stress, redirecting internal elastic stress toward the confining plate through out-of-plane rearrangements. Frictional forces at the boundaries quench the motion of these wedged-out particles. As a result, the rest of the cylinders lose mobility which in turn helps maintain the compressed state achieved from loading. The distinction between these compaction behaviors—one with no internal stress and another characterized by a nonzero residual stress, marks a dynamic transition from in-plane particle rearrangement to out-of-plane popping. The experimental need for a constituent material with low friction that would not topple under external loading operationally translated to the use of hollow rubber cylinders whose softness prevented toppling and the annular contact ensured low friction.

II. EXPERIMENTAL DETAILS

The experiments were conducted in a square shear cell (see Fig. 1) measuring 190 mm per side, containing a pack of co-axial rubber cylinders with heights of 12 mm and inner and outer diameters of 5.32 mm and 12.25 mm, respectively. This cell was sandwiched between two acrylic plates. The top plate, secured by springs, maintained a clearance gap ($H_0 = 16$ mm) to allow cylinder movement without popping out. A pneumatic shaft, connected to an air compressor, repeatedly struck the cell every 10 seconds, moving a distance of 160 mm before being brought to rest by a stopper (Fig. 1). This brought the system to its maximally strained state. The system's density ρ was varied by changing the number of cylinders in the assembly. ρ is defined as

$$\rho = N\pi R^2/A_{\text{comp}} = N\pi R^2/(L^2 \sin \theta_{\text{max}}),$$

*Contact author: bandi@oist.jp

†Contact author: sghosh@tifr.res.in

Published by the American Physical Society under the terms of the Creative Commons Attribution 4.0 International license. Further distribution of this work must maintain attribution to the author(s) and the published article's title, journal citation, and DOI.

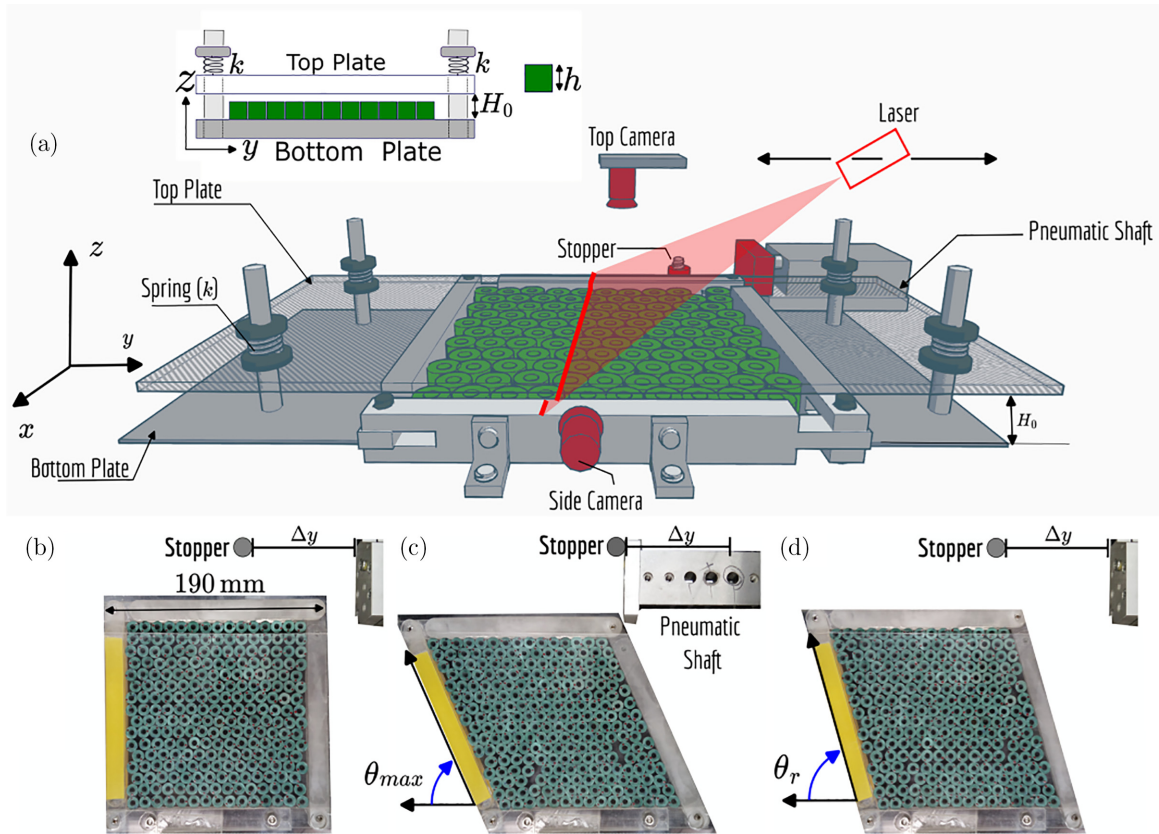


FIG. 1. Experimental setup schematic: (a) Illustration of the setup featuring rapid shear application and a 2D laser sheet projected onto the shear assembly to measure vertical movement and scan the granular pack’s height profile. Inset: Highlight of the gap between the top and bottom plates, with the top plate at resting position (H_0). (b)–(d) Top view of the shear assembly at different cycle stages: (b) initial, (c) after shear loading, and (d) relaxation post-loading. The yellow arm indicates the inclination of the system relative to the horizontal line aligned with the pneumatic shaft.

where N is the number of cylinders, A_{comp} is the area of the shear cell in the maximally strained configuration, L is the length of the shear cell arm, R is the radius of a cylinder, and θ_{max} is the angle (see Fig. 1(c)) formed by the shear cell side walls with the direction of shaft movement in the maximally strained state (with $\theta_{\text{max}} = 64.9^\circ$ which is the same for all experiments). For the density spanned in these experiments, the number of cylinders in the shear cell varied from 224 to 252.

After loading, the system relaxed to a new configuration. The impacts continued for 500 cycles under specific density and cylinder friction coefficients. Before each experiment, cylinder positions were randomized to eliminate memory effects from previous runs. Unless specified otherwise, all data presented were averaged over at least 8 – 10 independent experimental runs. For our experimental study, we used three different kinds of cylinders with ρ ranging from 0.8 to 0.92. All the cylinders were cut from nitrile butadiene green rubber pipes. To reduce the friction coefficient the cylinders were coated with glossy paint further lubricated by boric acid while for increasing friction, sandpapers of fine grit were pasted around the objects. Details about the method of friction measurement are provided in the Appendix.

Rapid shear loading at high densities caused the cylinders to move upward, compress the springs, and raise the

top plate. The force exerted by springs was quantified by monitoring the vertical displacement of the top plate using a side camera, while a camera mounted atop recorded the cell configuration and cylinder arrangement (see S3.avi [31]). A custom-built laser profilometer was used to construct the assembly’s surface profile $\zeta(x, y)$. Figures 1(b)–1(d) depict initial, post-shear loading, and post-relaxation positions for the first impact. The relaxed state density ρ_r is defined as $\rho_r = N\pi R^2/A_{\text{relx}} = \rho \sin \theta_{\text{max}}/\sin \theta_r$, where N is the number of cylinders, A_{relx} is the area of the shear cell in the relaxed state, and θ_r is the angle at which the shear cell relaxed in absence of loading. For a given ρ (or rather N), repeated impacts drove the system’s dynamic progression toward its most compact configuration. The compaction can be observed in Fig. 2(a) (top panel), where ρ_r is plotted for two representative densities. This gradual compaction resembles the slow relaxation process observed in vibrated granular systems [5,10].

III. RESULTS AND DISCUSSION

As the system became increasingly compact under repeated impacts, θ_r decreased eventually reaching a steady state fluctuating around an asymptotic angle $\theta_{r, \text{st}}$. θ_r is a measure of residual strain within the system. The normalized

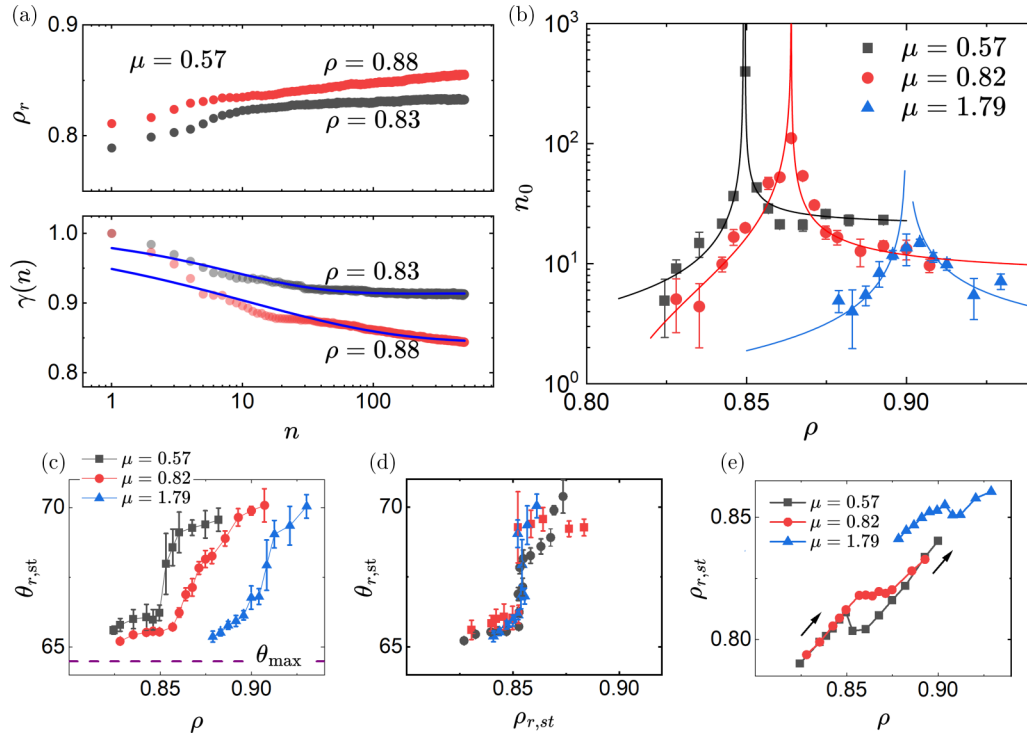


FIG. 2. Dynamical transition: (a) Top panel: Growth in relaxed density ρ_r . Bottom panel: Normalized residual strain $\gamma = \theta_r(n)/\theta_r(n=1)$ for $\rho = 0.83$ and $\rho = 0.88$, fitted with a stretched exponential function $(1 - \gamma_\infty) \exp(-(n/n_0)^\beta) + \gamma_\infty$ using parameters n_0 and γ_∞ . (b) Cycle constant n_0 versus ρ for friction coefficients $\mu = 0.57, 0.82$, and 1.79 , with power-law fits (exponent -0.75) and critical points at $\rho_c = 0.849, 0.864$, and 0.900 . (c) The relaxed steady-state angle $\theta_{r,st}$ is plotted for different friction coefficients, illustrating sharper transitions with lower friction. (c) Shows $\theta_{r,st}$ versus the steady state density $\rho_{r,st}$ for various μ , collapsing onto a single S-shaped curve. (d) $\rho_{r,st}$ is plotted with ρ , showing the effect of ρ and μ on the compaction.

residual strain is defined as $\gamma(n) = \theta_r(n)/\theta_r(n=1)$ and its evolution is plotted in Fig. 2(a) (bottom panel) for two representative densities ($\rho < \rho_c$ and $\rho > \rho_c$). Here ρ_c is a critical density associated with a dynamical transition, which is explained in detail later in the paper. Since, $\theta_r = \sin^{-1}(\rho \sin \theta_{\max}/\rho_r) = \theta_r(\rho, \rho_r)$, for a given ρ , the evolution of $\gamma(n)$ (or θ_r) is reflective of the compaction mechanism inside the system.

The parameter $\gamma(n)$ fits to a stretched exponential function:

$$\gamma(n) = (1 - \gamma_\infty) \exp(-(n/n_0)^\beta) + \gamma_\infty,$$

with γ_∞ and n_0 as fit parameters. Here, n_0 is the cycle-constant associated with each ρ , and the long-time saturation value is given by $\theta_{r,st} = \gamma_\infty \theta_r(0)$. The solid lines in the bottom panel of Fig. 2(a) represent the curve fits where β is the stretching exponent. Initially, the fitting was performed for β ranging from 0 to 1 for all the densities and the best fit was found for $\beta = 0.3 \pm 0.05$.

The cycle constant n_0 obtained from the fitting is plotted as a function of ρ (see Fig. 2(b)) for cylinders with varying friction coefficients $\mu = 0.57$ (black squares), $\mu = 0.82$ (red circles) and $\mu = 1.79$ (green triangles). The data show divergence at a friction-dependent critical density $\rho = \rho_c$. The strength of the frictional coupling significantly influences both the critical density ρ_c and the sharpness of the transition. A trend emerges where lower values of the friction coefficients correspond to more pronounced divergences and smaller ρ_c . The functional form $|\rho - \rho_c|^{-\nu}$, where $\nu \approx 0.75$, captures this

divergence well. This critical exponent is reminiscent of the temporal divergence observed in the relaxation of a quasistatically sheared mono-disperse disk packing [20].

Since $\theta_{r,st}$ is a measure of how much compaction has taken place, (more the $\theta_{r,st}$, less the compaction) we plot it against ρ for three friction coefficients. The plot shows a sharp rise beyond ρ_c for $\mu = 0.57$, whereas it gets smeared out for the highest friction studied. It also demonstrates that for an arbitrary $\rho > \rho_c$, higher friction results in greater compaction. Plotting $\theta_{r,st}$ against steady-state density (Fig. 2(d)) reveals a collapse of data onto a master curve (Fig. 2(d)) suggesting that irrespective of N or μ , the system needs an effective steady-state density $\rho_{r,eff} \simeq 0.85$ to exhibit the transition. It so happens that, to achieve the same $\rho_{r,eff}$, cylinders with higher interparticle friction need larger ρ_c compared to the lower friction cylinder assembly. Notably, the value of $\rho_{r,eff}$ draws close resemblance to the Random Close Packing density in 2D disordered media [21,22]. The plot in Fig. 2(e) illustrates the relationship between the steady-state density $\rho_{r,st}$ in the relaxed state and ρ , revealing two distinct compaction processes denoted by dashed lines. Initially, $\rho_{r,st}$ grows linearly with ρ but near the transition, for lower friction, the cylinders get wedged out of the 2D plane and touch the top plate. As a result, the system finds it difficult to rearrange in-plane resulting in a lower state of compaction. Since we keep on adding more cylinders, the compaction cannot stop. Therefore, it happens along a different line, beyond the critical point. On the other hand, cylinders

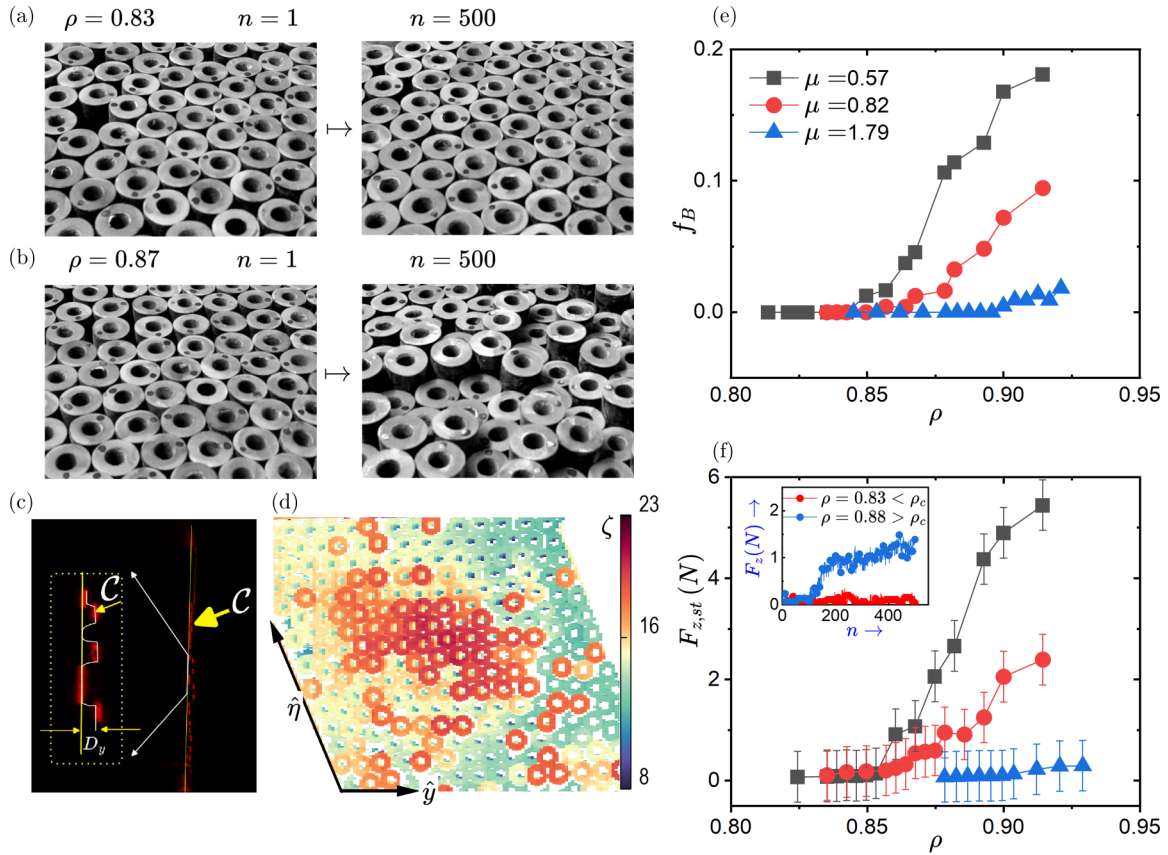


FIG. 3. Transition to the popped state: (a), (b) Slanted views of the granular assembly at $n = 1$ for densities $\rho = 0.83$ ($< \rho_c$) and $\rho = 0.87$ ($> \rho_c$) with $\mu = 0.57$. The right panels of (a) and (b) show corresponding steady-state configurations after 500 shear cycles. (c) Deviation (D_y) of the stripe (C) on the surface from a straight line due to cylinder elevation. (d) Representation of height $\zeta(x, y)$ using color in the image, with unit vectors $\hat{\eta}$ and \hat{y} along the shear cell's side and bottom walls (black boundary shown). (e) Fraction of popped-out cylinders (f_B) vs. ρ is plotted for three μ values. The number of popped-out cylinders is computed from the height profile obtained using the laser scanning profilometer. (f) Inset: Vertical force exerted on the top plate by the shear assembly plotted for densities $\rho = 0.83 < \rho_c$ and $\rho = 0.87 > \rho_c$, along with steady-state computations for different friction coefficients. The force increases beyond ρ_c for $\mu = 0.57$ and $\mu = 0.82$.

with higher friction do not pop out resulting in achieving a higher degree of compaction. The critical slowing down of the timescale observed in Fig. 2(b) has been extensively studied in various disordered media [23–26]. Our observation of a similar relaxation strongly points to the inherently disordered nature of our system. As we will detail shortly, even to start with, the cylinders' cross-sections were not exactly circular, giving rise to an inherent disorder in the system. Above the critical point, in the presence of mechanical constraints, this inherent disorder was amplified, accompanied by a fraction of cylinders popping out randomly from the 2D plane.

To investigate the nature of the disorder across the transition we captured snapshots of the granular shear assembly from a slanted view after the initial and final impact, as shown in Figs. 3(a) and 3(b). These images were taken in the post-loading state. The images show a distinct qualitative difference in the surface profile of the system below and above the critical density. Below the critical density, the system exhibited compaction through in-plane rearrangements of the cylinders (Fig. 3(a) and Movie S1.avi [31]). For $\rho > \rho_c$, the very first impact caused the cylinders to coherently buckle out of the 2D plane (see Movie S2.avi [31]). The

signature of this out-of-plane mechanical instability is also captured in the speed profile of the pneumatic shaft (see Fig. 12) during the first impact. Even after removing the external loads, the system's buckled state persisted, with certain cylinders remaining wedged out in the relaxed state. Subsequent loading cycles intensified the structural instabilities associated with the out-of-plane motion of the cylinders, increasing the probability of cylinders remaining in the popped state.

We quantified the number of popped-out cylinders using a Laser Scanning Profilometer. A 2D laser sheet was projected onto the shear assembly at a nonzero angle relative to the direction of gravitational acceleration, forming a stripe C along the x axis, see Fig. 3(c). The height at each y value was calculated as $h(y) = D_y(y) \tan \psi$, where $D_y(y)$ is the deviation along the negative y axis of C from a perfectly flat surface and $\psi = 45^\circ$ is the angle made by the laser sheet with the xy plane. The height resolution of this method is about 2 mm, this is mainly set by the width of the laser sheet. The height resolution of this method is approximately 2 mm, which is about 16% of the size of the cylinders. This resolution is primarily determined by the width of the laser sheet.

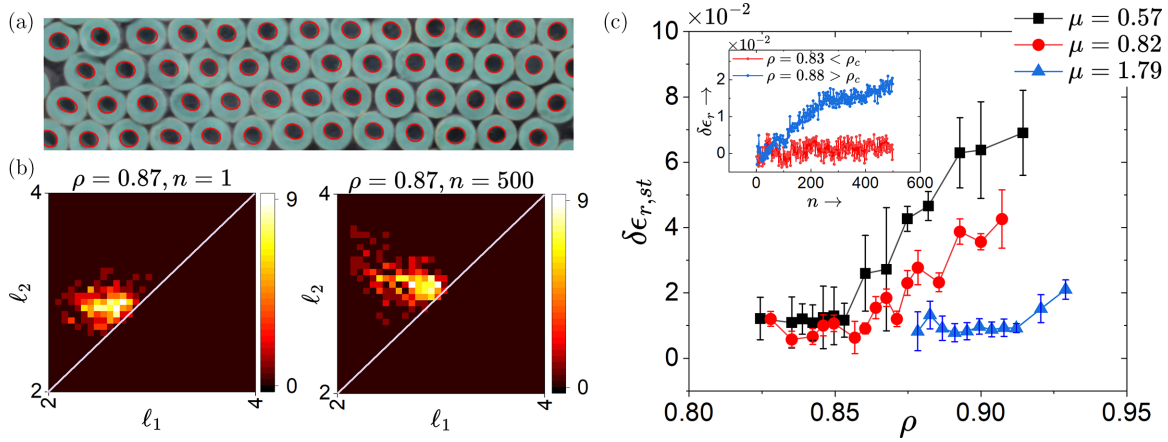


FIG. 4. Disorder in shape: (a) Ellipses fitted to internal contours of cylinder cross-sections illustrate fit quality in this plot. (b) Bivariate histograms of the system in a relaxed state, displaying distributions of semi-major (ℓ_2) and semi-minor (ℓ_1) axes of inner elliptical contours for cylinder cross-sections at $\rho = 0.87$. The left plot is at $n = 1$, and the right one is in the steady state, $n = 500$. The solid lines, $\ell_2 = \ell_1$, represent the points corresponding to circular cross-sections. (c) Steady-state values $\delta\epsilon_{r,st}$ are shown as functions of ρ for three different friction coefficients. Inset: Change in average eccentricity ($\delta\epsilon_r = \langle\epsilon_r\rangle - \langle\epsilon_{r,1}\rangle$) plotted for two representative densities.

To study the height profile $\zeta(x, y)$ of the assembly, the laser was incrementally translated along the negative y axis, causing \mathcal{C} to sweep across the shear cell length. The top camera captured \mathcal{C} images on the cylinder surface. Fig. 3(d) shows a typical height profile, where colors represent cylinder heights in mm. Cylinders over 16 mm in height are considered popped-out of the 2D plane. The plot in Fig. 3(e) shows the evolution of the popped state (measured by the fraction of popped-out cylinders, f_B) as a function of density ρ for three different μ . Increasing friction leads to a less distinct transition, indicating that higher interparticle friction stabilizes the planar arrangement of cylinders, making it difficult for them to pop out.

To measure the confining force exerted by the popped-out cylinders beyond ρ_c , the combined spring constant of the springs attached to the top plate was multiplied by the plate's vertical displacement, which was monitored using the side camera. Details of the method of measuring the spring constant are given in the Appendix. Inset in Fig. 3(f) plots the vertical force $F_z(N)$ as a function of n for two representative densities ($\rho < \rho_c$ and $\rho > \rho_c$). It shows that beyond ρ_c , after a few initial impacts, $F_z(N)$ starts rising, eventually reaching to a steady state. We plot the average vertical force $F_{z,st}$ exerted in the steady state as a function of ρ . It shows a transition at $\rho = \rho_c$ corresponding to their respective friction coefficients. Interestingly, $F_{z,st}$ reduced significantly for any arbitrary $\rho > \rho_c$, suggesting higher friction causing lesser internal stress.

The radial deformation of the cylinders is a measure of local stress in the system. To quantify this deformation, we measured the eccentricity of the internal contour of the top annular region of each cylinder. Coordinates of the internal contours were detected and an equation of ellipse was fitted to these coordinates. Figure 4(a) shows a small patch of the system depicting the quality of fits. Further details about detecting the eccentricities are given in the Appendix. Ideally, without any deformation, the cross-section of each

cylinder should be circular. However, at the outset of the experiment, the cross-sections of the cylinders were measured to be slightly elliptical rather than circular, exhibiting an average residual eccentricity $\langle\epsilon_{res}\rangle \sim 0.38$. The bivariate histogram of the semi-major (ℓ_2) and semi-minor axes (ℓ_1) of the cylindrical cross-sections are plotted in Fig. 4(b) for $n = 1$ and $n = 500$ in the relaxed state. The quoted densities are determined by approximating these elliptical cross-sections as circular, introducing an error of $\delta\rho = \pm 0.01$. Inset of Fig. 4(c) demonstrates the average eccentricity at an instance minus the average eccentricity at $n = 1$, $\delta\epsilon_r = \langle\epsilon_r\rangle - \langle\epsilon_{res}\rangle$ as a function of n for two representative densities ($\rho < \rho_c$ and $\rho > \rho_c$). While $\delta\epsilon_r$ remains almost constant for $\rho < \rho_c$, it increases and finally saturates in the steady state at $\rho > \rho_c$. This internal stress building up can be further understood by plotting the steady state value of $\delta\epsilon_{r,st}$ against ρ . It is observed that similar to the vertical stress developed in the system, the average radial deformation also gets enhanced beyond ρ_c for $\mu = 0.57$ and $\mu = 0.82$ but does not show a significant increase for $\mu = 1.79$. High interparticle friction destroys the internal stress retained in the system, resulting in a more compact configuration. This type of disorder aligns with studies on properties of systems with very low polydispersity [27,28].

To gain insights into the mechanisms of cylinder popping and the rotational motions associated with in-plane rearrangement and out-of-plane popping, we individually marked and tracked each cylinder over time. Figure 5(a) shows the average absolute angular displacement $|\Phi(n)|$ for three densities, showing the characteristics of the power law with n . $|\Phi(n)|$ is defined as $|\Phi(n)| = \langle|\Theta(n)|\rangle - \langle|\Theta(n=1)|\rangle$, where $\langle|\Theta(n)|\rangle$ is the average orientation of the cylinders. The plot indicates the absence of a state where all rotational activity ceases (see Appendix, Fig. 14(b)). In Fig. 5(b), the final $|\Phi_f|$ against ρ reveals a maximum at $\rho = \rho_c$, suggesting increased cylinder rotation propensity at the transition density. Below ρ_c , particle rotations involve sliding during in-plane particle rearrangement, while above ρ_c , in-plane rotations are

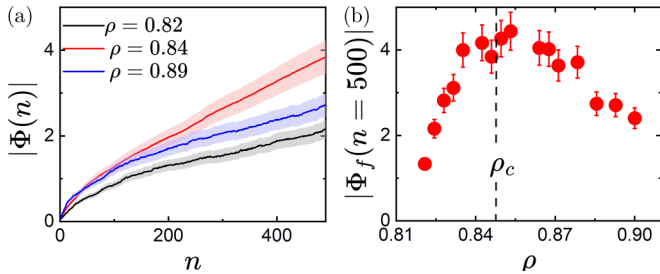


FIG. 5. Particle rotation: (a) Shows the variation of the average absolute angular displacement per particle $|\Phi(n)|$ with n for three representative densities ($\rho < \rho_c$, $\rho = \rho_c$, and $\rho > \rho_c$). All the data show a power law behavior with respect to n . In (b) we plot $|\Phi_f|$, i.e., the average absolute angular displacement at the final cycle as a function of ρ . It shows a maxima at $\rho = \rho_c$. The friction coefficient μ between the cylinders in this experiment is 0.57.

complemented by screw-type motions extending out of the plane (see S3.avi [31]).

IV. CONCLUSIONS

In this paper we have shown that the reconfiguration of particles due to mechanical instabilities leads to a popped state, directing stress toward the confining walls. Furthermore, we demonstrate a dynamical transition between non-popped and popped states during the process. Interparticle friction stabilizes the non-popped state, isolating it from the influence of boundary friction. By increasing friction between particles, one can smoothen this transition, influencing the overall behavior of the system. The paper establishes that the mechanical response of a system can be effectively controlled by adjusting its relaxation time or particle mobility. Typically, this control involves modifying an external parameter within the system, such as temperature in the context of glasses [29], which alters molecular mobility and consequently increases relaxation time. In the present context, popping hinders particle mobility by introducing frictional constraints from boundaries, which arise as individual particles reorganize during compaction. It is via these additional frictional forces, that the system can significantly increase the system's relaxation time. This paper does not address the effect of system size dependence on the transition, however, that is a question better answered by numerical studies.

ACKNOWLEDGMENTS

M.M.B. was supported by the Nonlinear and Nonequilibrium Physics Unit, OIST Graduate University. The authors thank D. Levine, N. Goldenfeld, and M. Venkadesan for feedback and acknowledge the International Centre for Theoretical Sciences (ICTS) for hosting during the program - Soft and Living Matter: from Fundamental Concepts to New Material Design (code: ICTS/SLM2023/8), when parts of this work were undertaken. S.G. acknowledges the support of the Department of Atomic Energy and Science and Engineering Research Board, Government of India, under Projects No. 12-R&D-TFR-5.10-0100 and No. CRG/2020/000507.

APPENDIX A: EXPERIMENTAL SETUP

1. Granular particles

We used coaxial rubber cylinders as soft granular particles. These cylinders were cut from nitrile butadiene green rubber pipes and had the following dimensions: an inner diameter of 5.32 mm, an outer diameter of 12.25 mm, and a height of 12 mm. Hollow cylinders were used because the experimental requirement was to use soft material that could get pushed without toppling. Unfortunately, most soft materials also have high friction. If the friction is too high, it could result in mechanical instability and cause the cylinders to topple. Thus, it is crucial to balance the softness of the cylinders and the friction between them and the bottom substrate. The chosen cylinders represent a solution in this regard. Their hollow nature imparts softness, and since only the annulus makes contact with the substrate, they exhibit low friction.

2. Controlling interparticle friction

The experiments involved adjusting the friction between the cylinders using three different approaches: The first involved using the original cylindrical rubber tubes with their natural friction coefficient ($\mu = 0.82$). The second approach employed rubber tubes coated with glossy paint and further lubricated with boric acid to decrease the friction coefficient ($\mu = 0.57$). Lastly, rubber tubes were wrapped with fine-grit sandpaper (180) to increase the friction coefficient ($\mu = 1.79$). The friction coefficients of the cylinders were measured using the method described by Bandi *et al.* [17].

3. Measurement of the friction coefficient

The experimental setup for measuring friction is depicted in Figs. 6(b) and 6(c). Four rubber cylinders are arranged in contact, with three outer cylinders fixed in place and unable to move or rotate. The middle cylinder is connected to an axle that is linked to a pair of pulleys. This setup allows the middle cylinder to rotate by applying torque through weights (W) suspended from the pulleys (P_1, P_2). An external force (F_a) is applied to the top cylinder using an indenter connected to a load cell, which measures the force exerted by the indenter. The load cell generates a voltage corresponding to this force, which can be converted into actual forces using a calibration curve. The calibration curve is shown in Fig. 9(a). The bottom cylinders, positioned at angle $\theta = 30^\circ$ with respect to gravity, also exert an equal force F_b on the middle cylinder. Thus, the total normal force acting on the middle cylinder is

$$F_N = F_a + 2F_b.$$

In mechanical equilibrium, $F_a = 2F_b \cos \theta$, thus

$$F_N = F_a + F_a / \cos \theta.$$

Applying a tangential force F_T on the middle cylinder allows it to slip at a critical force, enabling the determination of the static friction coefficient $\mu = F_T / F_N$ for the cylinders. This tangential force F_T is generated by the torque from the weights W suspended from P_1 and P_2 . Using torque balance, we find $F_T = WR/r$, where r is the radius of the cylinder and R is the pulley radius. Once F_T is known, the friction coefficient can

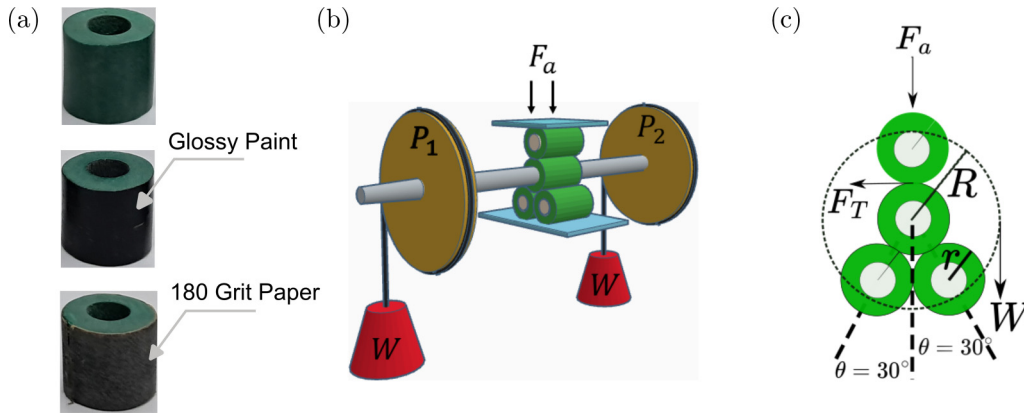


FIG. 6. Panels in (a) show representative photographs of the cylindrical particles of varying friction coefficients. The top one is of intermediate interparticle friction whereas the middle and the bottom one correspond to lowest and highest friction coefficients. The top one has an interparticle friction coefficient of $\mu = 0.82$. In the middle, the particle is coated with glossy black oil paint. To reduce friction further, the entire assembly was lubricated with boric acid, reducing the interparticle friction coefficient to $\mu = 0.57$. Sandpaper with a grit of 180 was pasted around the objects to increase friction. This enhanced the friction coefficient to $\mu = 1.79$. A representative image of a cylinder wrapped in fine-grit sandpaper is shown at the bottom of (a). The experimental setup to measure friction is schematically shown in (b). The schematic view of the cross-section of the cylinder assembly with force diagrams are depicted in (c).

be calculated using the formula

$$\mu = \frac{F_T}{F_a(1 + 1/\cos\theta)} = \frac{WR/r}{F_a(1 + 1/\cos\theta)}.$$

4. Quantifying the cross-section of the cylinders

Notably, at the outset of the experiment, the cross-sections of the cylinders were elliptical rather than perfectly circular, exhibiting a nonzero eccentricity in the system. To ensure accurate measurement of the eccentricity of the cylinder cross-sections, precautionary measures had been taken. The bottom sheet had been painted black, and bright light sources were strategically positioned above the assembly to illuminate the upper annular region of the cylinders. This specific lighting arrangement was designed to eliminate the visibility of the vertical inner walls of the cylinders in captured images, effectively preventing any interference with the process of ellipse detection. For a system with N cylinders, the center and eccentricity of each cylinder were located and estimated through the following procedure. First, the green channel of the image was binarized, and a Canny edge filter was applied to detect the inner and outer boundaries of the annular region of the cylinders. Subsequently, all closed contours in the thresholded image were recognized to identify each cylinder. Classifiers such as convexity, area, and perimeter length were used to distinguish contours representing the inner edge of a cylinder. The method of least squares, as detailed in [30], was then employed to determine the equation of the ellipse that best fit the set of 2D data points corresponding to each selected closed contour. This procedure provided estimates for the center, C_i , and eccentricity, ϵ_i , of the cross-section of each cylinder, where $i = 1 \dots N$. The fitted ellipses are shown as red contours in Fig. 7.

5. Quantification of cylinder orientations

To track the orientation of each cylinder around its own axis, a red patch was applied to its annular region. An example

of this red patch on the cylinder’s annular region is depicted in the inset of Fig. 7. The center (P_i) of this patch was then located. The angle formed by the line connecting C_i and P_i with the y-axis determined the orientation angle (Φ_i) for the i -th cylinder. These lines (C_iP_i) are represented as red straight lines in Fig. 7.

6. Shear cell

The shear cell, housing these cylinders, consisted of four arms (190 mm \times 20 mm \times 14 mm) and was placed on a rectangular acrylic sheet. The sheet was attached to the experimental table, and one arm of the shear cell was fixed onto the acrylic plate, while the other three arms could move,

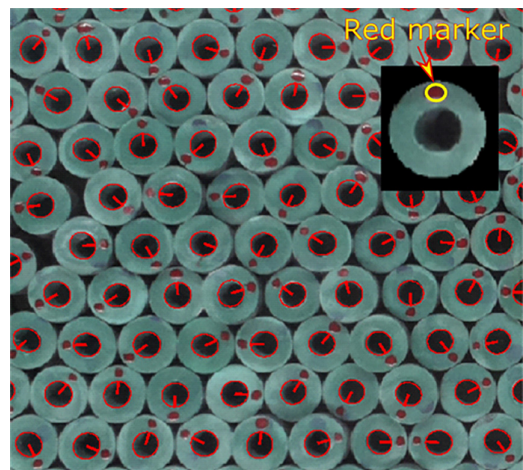


FIG. 7. The cross-sections of the cylinders are quantified by fitting ellipses (marked in red) to the inner circumference of the cylinders. The red patch (P) marked on the annular part of the cylinder is used to determine its instantaneous angular position. Radial straight lines connect the center of the red patch to the center (C) of the cylinder.

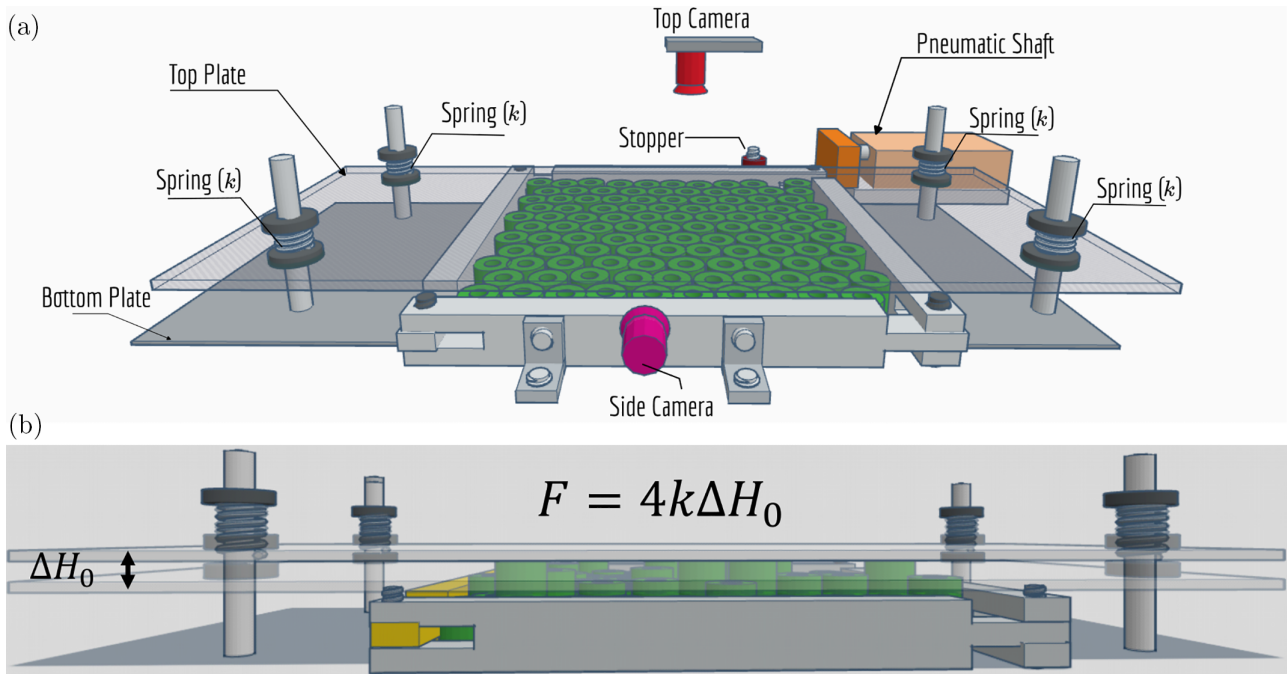


FIG. 8. The panel (a) illustrates the schematics of the experimental setup. Panel (b) schematically depicts the displacement of the top plate in response to the particles popping out of the plane.

ensuring that parallel arms remained parallel at each instantaneous stance of the shear cycle (see Fig. 1(b)–1(d) for three representative stances). Before the experiments commenced, cylinders were randomly placed with their axes perpendicular to the bottom plate. The density (ρ) was defined as the ratio of the area occupied by those cylinders to the maximum area of the shear cell in its fully sheared configuration. For the density spanned in these experiments, the number of cylinders in the shear cell was varied from 224 to 252. The system was kept horizontal, and a transparent acrylic sheet (486 mm \times 200 mm \times 6 mm) was attached to prevent runaway instability and maintain a constant number of cylinders. A camera (v2-8MP) was mounted atop the shear assembly to capture images throughout the experiment (see Fig. 1(a)) with a resolution of ~ 6.53 pixels/mm. A more detailed schematic of the experimental setup is given in Fig. 8.

7. Measurement of the normal force F

Four identical metallic springs (ID = 15 mm, OD = 16.5 mm, height = 35 mm, stiffness constant $k = 0.621 \pm 0.006$ N/mm) were clamped to steel rods (12 mm diameter) at the plate corners (see Figs. 1(a), 8(a), and 8(b)). Spring stiffness coefficients were measured by attaching the spring to a load cell connected to a linear motorized stage, and displacement was controlled while voltage was measured using a multi-meter. Calibration data for force and voltage of the load cell was used to compute spring stiffness. Additional details, including calibration data, are provided in the Fig. 9.

A plexiglass piece (66 mm \times 53 mm \times 3 mm) with a marked black line was attached perpendicularly to the top plate. The line’s movement was monitored by a second camera (v2-8MP) mounted sideways to measure the top plate’s height change with a resolution of ~ 59 pixels/mm. To move upward,

cylinders must overcome the stiffness of the springs clamped to the steel rods above the top plate. The vertical force F exerted by the system was the effective spring constant ($K = 4k = 2.484$ N/mm) multiplied by the vertical displacement ΔH_0 of the springs (and thus the top plate), i.e.,

$$F = 4k\Delta H_0.$$

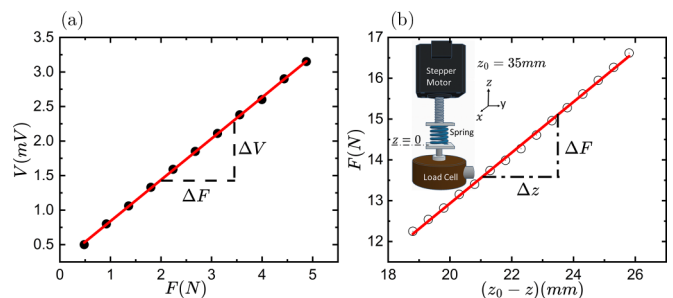


FIG. 9. (a) The calibration curve of the load cell (SYNAPSIS TECHNO INDUSTRIES, MODEL-LZYA, 0-5KG) is generated by the following method. An object of a nonzero mass is suspended from the load cell and the voltage generated due to the weight of the object is recorded. The object mass is varied in multiple of a finite mass (11.2 g). Slope ($\Delta V/\Delta F$) of the curve is 0.597 ± 0.003 . (b) Inset: The schematic diagram of the spring measurement apparatus. The spring is sandwiched between a linear translator stage connected to a stepper motor and the load cell. The motorized stage moves in the $-ve z$ direction. As a result, the spring gets compressed and exerts a resistive force in the opposite direction. This force is measured in terms of voltage generated by the load cell. From the calibration curve, the voltage can be converted into force. Slope of the $F(N)$ vs. $(z_0 - z)$ (mm) curve is the stiffness constant ($k = 0.621 \pm 0.006$ N/m) of the spring. z_0 (= 35 mm) is the length of the spring without any externally applied force.

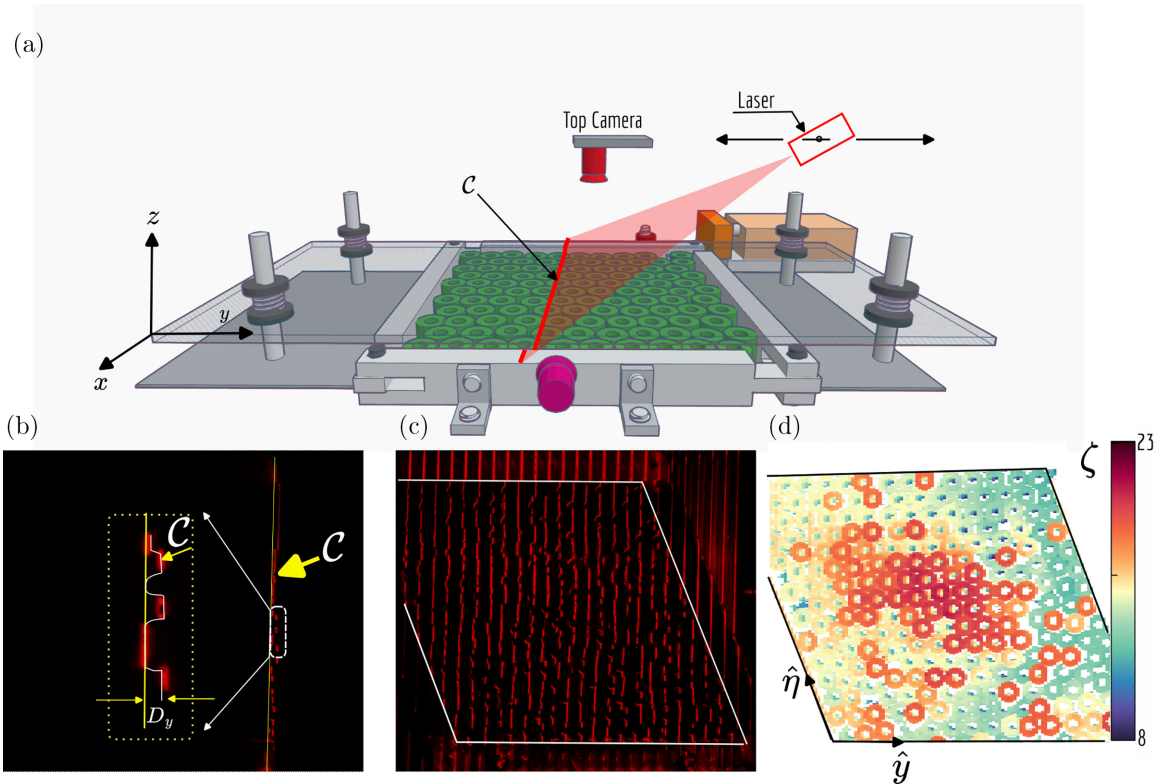


FIG. 10. Laser Scanning Profilometry: (a) Schematic diagram of the custom-built scanning 2D laser stripe profilometer. A 2D laser sheet projected onto the surface of the cylinders makes a red stripe C . The plane of the laser sheet makes an angle of 45° with the xy plane. The laser, connected to a stepper motor, incrementally moves across the system along the y axis, this causes the stripe C to sweep across the length of the shear cell. At each step, the top camera captures an image of the laser stripe C on the surface of the cylinders. (b) The stripe (C) on the surface forms a curve due to finite height of the cylinders. Height can be calculated from the angle at which the laser is projected onto the surface using the formula: $h = D_y \tan \theta$, where D_y is the deviation of C from the imaginary straight line that would have formed on a perfectly flat surface. To study the height profile $\zeta(x, y)$ of the complete assembly, the laser is systematically traversed along the y -axis in incremental steps. At each laser position, an image of the laser stripe on the assembly of the rubber cylinders is captured. Once the laser stripe has traversed the entire assembly, a sequential stack of these images is compiled. A composite image as shown in panel (c) is subsequently generated from this stack by projecting the maximum intensity in the direction of the stack. A white line is delineated to indicate the inner boundary of the cell. (d) Height ζ at each (x, y) coordinate is represented by a heat map in the image. Any of the cylinders which has elevation more than the height of the shear cell wall (16 mm), is defined as popped-out cylinder in our experiment. The unit vectors $\hat{\eta}$ and \hat{y} point along the side and bottom wall of the shear cell (shown by the black boundary).

8. Residual strain measurement

To quantify the angle θ between the shear cell and the impact direction, one side arm of the shear cell was colored in yellow for easy identification (see Fig. 1). The image was processed by subtracting the blue channel from the green to isolate non-zero pixels in the yellow-colored region. Canny edge detection was then employed to identify the edge of the colored side arm. Subsequently, Hough transformation was utilized to identify the slope m of this edge, and thus

$$\theta = \pi - \arctan(m).$$

9. Height profile measurement

To analyze the height profile of the configuration, we utilized a custom-built scanning 2D laser stripe profilometer. Its schematic representation is shown in Fig. 10. In this method, a 2D laser sheet was projected onto the system at a 45-degree angle. The laser, connected to a stepper motor, incrementally

moved across the system along the y axis. At each step, the top camera captured an image of the laser stripe on the surface of the cylinders. On a flat surface, the laser stripe formed a straight line. When the cylinders moved out of the plane, this laser stripe deviated from the reference line and began to represent a curved line. The estimation of the vertical motion of each cylinder was determined by measuring the deviation of the laser stripe from its reference straight line. Analyzing this deviation enabled the construction of the height profile $\zeta(x, y)$ for the configuration. We defined those cylinders to be buckled, which had an elevation of about 16 mm.

APPENDIX B: EXPERIMENTAL PROCEDURE

For a fixed number of cylinders, the shear assembly was slammed by a pneumatic shaft connected to an air compressor, for 2 seconds and the external force was removed to let the system relax for 10 seconds. Air pressure in the compressor was kept fixed at 5 bars throughout the experiment. Motion

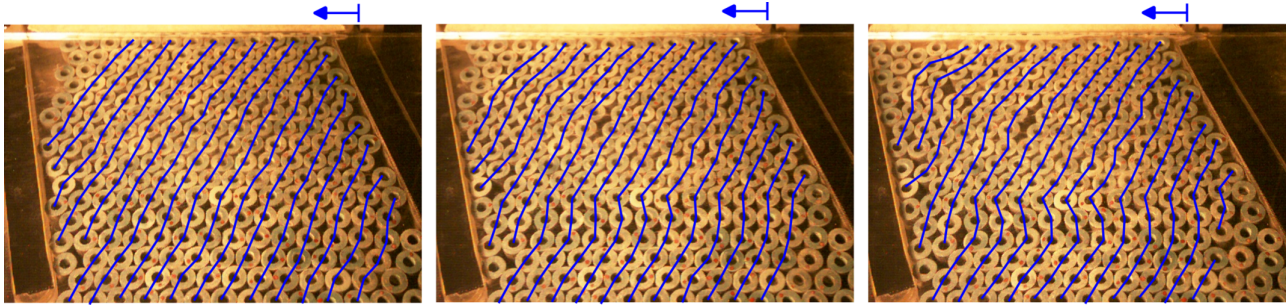


FIG. 11. In-plane buckling: These images correspond to frames 30 to 46 in the movie sequence (Movie S1.avi [31]), with a 4-frame interval, and show instances of in-plane buckling.

of the pneumatic shaft was controlled by a microprocessor called Raspberry PI. The Raspberry PI that we used was of 4 GB RAM and 2.5 GHz processor speed. It was connected to a camera (Raspberry PI built in Camera Module, V2-8 MP) at the top. The side camera was connected to another Raspberry PI of similar specifications. To simultaneously capture snapshots, the standard parallel processing protocol MPI (Message Passing Interface) was employed using the mpi4py Python module, installed on both of these microprocessors. Following the installation, the machinefiles containing IP addresses of these microprocessors was created on each of them. To facilitate remote communication with these Raspberry PIs, the secure shell protocol (SSH) was enabled.

For secure and password-less login, the Rivest-Shamir-Adleman (RSA) encrypted public and private keys were generated and shared between the Raspberry PIs. This enabled secure access to the microprocessors without the need for passwords during remote communication. The cameras captured the top and side views of the system respectively, before and after completion of each shear cycle.

All experiments were started from random initial configurations and all of them ran for 500 shear cycles. Before each experimental run, the system was vigorously shaken to ensure that no memory of the previous experiment was retained by the configuration.

APPENDIX C: SIGNATURES OF IN-PLANE AND GLOBAL BUCKLING

The response to the initial impact on the granular assembly was observed using a high-speed camera (PHANTOM/AMETEK, MIRO-M310) mounted sideways to the system. These videos provide direct evidence of in-plane and global buckling in the system. Below the critical density, the system exhibited compaction through in-plane rearrangements of the cylinders (Movie S1.avi [31]). However, for $\rho > \rho_c$, the very first impact caused the cylinders to coherently buckle out of the 2D plane (Movie S2.avi [31]).

1. In-plane buckling

The three images in Fig. 11 are from the film S1.mov, capturing instances of in-plane buckling in a collection of

load-bearing linear structures in response to shear deformation. The direction of the shear deformation is indicated by arrows. These images correspond to frames 30 to 46 in the movie sequence [31], with a 4-frame interval. The blue line in the first image represents a linear force chain, which undergoes buckling over time. Similar in-plane buckling events result in significant particle rearrangements observed towards the end of the movie [31].

In addition, the system's response to the pneumatic shaft impact is analyzed through two aspects: (1) examining the velocity profile of the shaft and (2) investigating the assembly's height profile.

2. Velocity profile of the shaft after initial impact

In Fig. 12(a), the pneumatic shaft's velocity magnitude (v_y) is plotted against time for various densities, revealing two distinctive velocity peaks. The first peak marks the point of maximum shaft velocity during collision with the shear cell, followed by a rapid deceleration phase as the particulate configuration undergoes compression at nearly 5 bars. The system undergoes a cycle of acceleration and deceleration in about 150 ms before the pneumatic shaft resumes acceleration (indicated by a vertical black arrow in Fig. 12(a)). The first velocity peak is universal, dependent on the physical characteristics of the pneumatic shaft. However, a smaller secondary peak follows, representing the pack's response to intense compression and indicating the pack's rejuvenation from yielding in constituent coaxial cylinders. The temporal separation between the secondary peak and the post-slammng deceleration phase hinders the system from adaptation during shear loading. Yielding, recorded through shaft speed (v_y), is short-lived and uniform at low densities but extends longer for densities exceeding ρ_c . Supplementary movies (S1.avi, S2.avi) qualitatively evidence this behavior, with yielding visible at higher densities in S2.avi due to its stretched-out time profile, as quantitatively shown in Fig. 12(a).

3. Height profile of the assembly after first impact

To quantify the distinction around the critical density ρ_c , we plot the height profile $\zeta(y)$ of the coaxial cylinder system after the first shear loading for various densities in Fig. 12(b). Minimal height deformations are observed at densities $\rho < 0.864$, while densities $\rho > 0.864$ exhibit

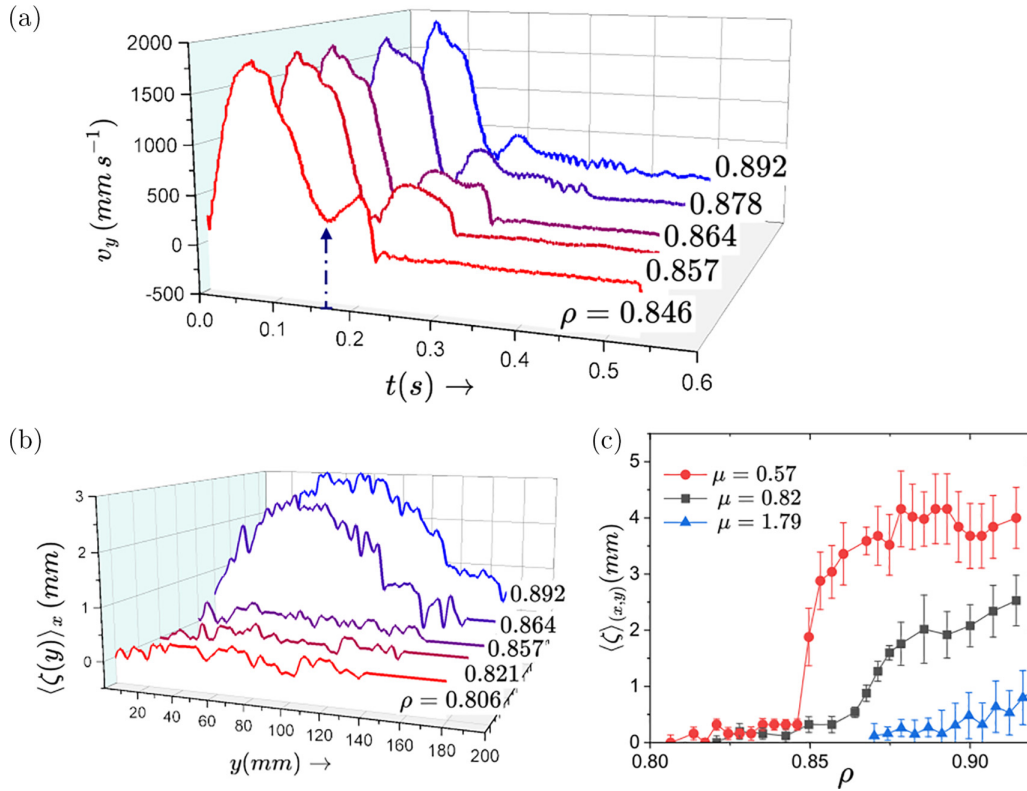


FIG. 12. (a) Temporal variation of pneumatic shaft velocity for representative densities ρ at friction coefficient $\mu = 0.82$. (b) Height profile of hollow cylinders $\langle \zeta(y) \rangle_x$ averaged along the x axis, immediately after the first shear loading for various densities. Global buckling is evident from the data of continuous deformation for $\rho > \rho_c$. (c) Variation of average height profile $\langle \zeta \rangle_{x,y}$ with ρ for three friction coefficients ($\mu = 0.57, 0.82, 1.79$).

characteristic out-of-plane bowing, indicating continuum slender body buckling. We operationally identify the critical density as $\rho_c = 0.864$. Distinct instability mechanisms below and above ρ_c result from interparticle friction. Friction constrains rotational degrees of freedom, causing coaxial cylinders to behave like a continuum solid and buckle out of plane above ρ_c . This is supported by Fig. 12(c), where we plot $\langle \zeta \rangle_{x,y}$, the averaged height profile inside the shear cell, for three friction coefficients. Firstly, ρ_c —the density where $\langle \zeta \rangle_{x,y}$ starts rising above 0 mm—shifts to higher densities with increasing friction coefficients, confirming the role of friction in the dynamical transition. Secondly, the magnitude of the jump in $\langle \zeta \rangle_{x,y}$ becomes smoother and more gradual with increasing friction coefficient μ , suggesting that friction stabilizes the pack against mechanical failure and smoothes out the transition.

APPENDIX D: DENSIFICATION OF THE SYSTEM

Upon repeated impacts, the system begins to densify. The degree of densification achievable depends on the coefficient of friction between the cylinders. A system with lower interparticle friction attains lower density due to mechanical instability when a critical density is exceeded. This instability causes the cylinders to pop out of plane, enhancing the friction interaction between the popped-out cylinders and the wall. This increased frictional interaction limits the in-plane motion

of the cylinders, hindering the densification process. Figure 13 shows the growth in the density ρ_r of the system in its relaxed state, i.e., $\theta = \theta_r$ with the number of impacts for three different *a priori* densities, ρ , of the cylinders in the shear cell. The data is presented for three different friction coefficients between the cylinders: (a) $\mu = 0.57$, (b) $\mu = 0.82$, and (c) $\mu = 1.79$. The *a priori* density, ρ , of the cylinder-assembly is measured in the maximum-shear loading state of the shear cell, $\theta = \theta_{\max}$.

APPENDIX E: PERSISTENT ROTATIONAL ACTIVITY

In conventional Cauchy mechanics, which deals with continuous elastic materials, the relative deformations among individual constituents—a characteristic response in granular solids—are not considered. However, both continuum and granular solids can experience sudden shape changes, known as structural instabilities. Buckling of slender structures is a common instability in Cauchy solids, analyzed using linear stability methods. However, in granular solids, neighboring particles can undergo different rearrangements under external loading, like shear band formation, leading to mechanical instability at the constituent level rather than the system scale.

In our experiments, we observed that individual cylinders started rotating during the loading phase, and this rotation does not get undone during the relaxation phase. As the

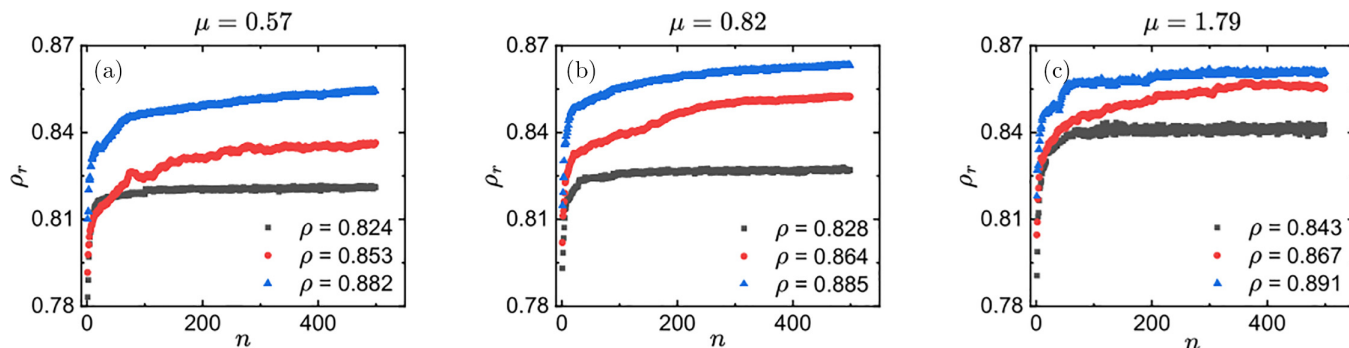


FIG. 13. Relaxed State Density with number of impacts: The figure depicts the growth in the density ρ_r of the system in its relaxed state, i.e., $\theta = \theta_r$ with the number of impacts for three different *a priori* densities, ρ , of the cylinders in the shear cell. The data is presented for three different friction coefficients between the cylinders: (a) $\mu = 0.57$, (b) $\mu = 0.82$, and (c) $\mu = 1.79$. The *a priori* density, ρ , of the cylinder-assembly is measured in the maximum-shear loading state of the shear cell, $\theta = \theta_{max}$.

system became denser, the fraction (f_R) of cylinders exhibiting persistent rotation decreased with increasing impact number (n) until it reached a saturation value (f_R^s). The highest fraction of rotating particles was observed at the critical density. In Fig. 14(a) we plot the fraction of rotating cylinders, f_R , against the impact number n for three representative *a priori* densities, ρ . Over successive impacts, f_R initially decreases but eventually saturates to a nonzero steady-state value, f_R^s .(b) The fraction of rotationally active cylinders in the steady state, $\langle f_R^s \rangle$, exhibits a peak near the critical density ρ_c . Averaging is performed over the last 100 cycles. A cylinder is considered rotationally active if its angular displacement in the relaxed state between two consecutive impacts is greater than 0.1 radians. We are not claiming that there is a divergence in rotational activity. Rather, we aim to show that rotational activity increases at the critical density. In fact, the presence of the top plate prevents any possibility of divergence, as a cylinder that pops up and touches the top plate cannot rotate further.

APPENDIX F: ERROR ANALYSIS

For the data presented in Fig. 12(c), the average was taken over the length of the laser line and the error bar presented was the standard deviation of these averages for various initial configurations divided by the square root of the total number of initial configurations.

We explained the error analysis for the Fig. 4(c), the increase in average eccentricity $\delta\epsilon_{r,st}$ plot as an exemplar, the remainder of the plots in Figs. 2 and 3, i.e., n_0 , $F_{z,st}$, and $\theta_{r,st}$ followed the same procedure. Between 8 to 10 independent experimental runs were conducted for each ρ , and for each experimental run the mean eccentricity of the cylinders in the shear cell was computed for the last 100 shear cycles (these are all steady state cycles). Therefore, there were average eccentricities for various initial configurations corresponding to a specific density. The error bar was calculated as the standard deviation of these average eccentricities divided by the square root of the number of initial configurations.

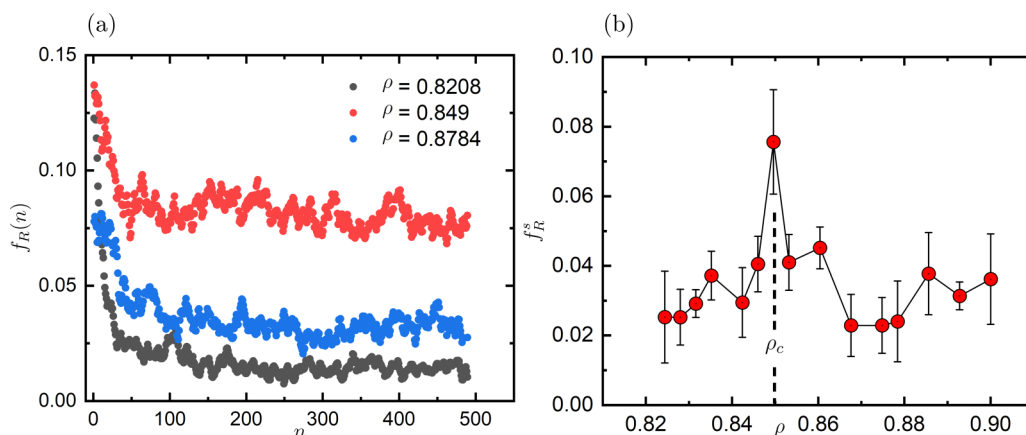


FIG. 14. Persistent rotational activity: (a) The plot illustrates the fraction of rotating cylinders, f_R , against the impact number n for three representative *a priori* densities, ρ . Over successive impacts, f_R initially decreases but eventually saturates to a nonzero steady-state value, f_R^s . (b) The fraction of rotationally active cylinders in the steady state, $\langle f_R^s \rangle$, exhibits a peak near the critical density ρ_c . Averaging is performed over the last 100 cycles. A cylinder is considered rotationally active if its angular displacement in the relaxed state between two consecutive impacts is greater than 0.1 radians.

- [1] S.-J. Feng, K. Tan, W.-H. Shui, and Y. Zhang, Densification of desert sands by high energy dynamic compaction, *Engineering Geology* **157**, 48 (2013).
- [2] G. A. Leonards, R. D. Holtz, and W. A. Cutter, Dynamic compaction of granular soils, *J. Geotech. Eng.* **106**, 35 (1980).
- [3] G. Alderborn and C. Nystrom, *Pharmaceutical Powder Compaction Technology* (Marcel Dekker, Inc., New York, 1996).
- [4] D. M. Wood, *Soil Behaviour and Critical State Soil Mechanics* (Cambridge University Press, New York, 1990).
- [5] P. Richard, M. Nicodemi, R. Delannay, P. Ribiere, and D. Bideau, Slow relaxation and compaction of granular systems, *Nat. Mater.* **4**, 121 (2005).
- [6] N. Iikawa, M. M. Bandi, and H. Katsuragi, Sensitivity of granular force chain orientation to disorder-induced metastable relaxation, *Phys. Rev. Lett.* **116**, 128001 (2016).
- [7] T. Vogler, M. Lee, and D. Grady, Static and dynamic compaction of ceramic powders, *Int. J. Solids Struct.* **44**, 636 (2007).
- [8] N. Iikawa, M. M. Bandi, and H. Katsuragi, Force chain evolution in a two-dimensional granular packing compacted by vertical tapings, *Phys. Rev. E* **97**, 032901 (2018).
- [9] N. Iikawa, M. M. Bandi, and H. Katsuragi, Structural evolution of a granular pack under manual tapping, *J. Phys. Soc. Jpn.* **84**, 094401 (2015).
- [10] J. B. Knight, C. G. Fandrich, C. N. Lau, H. M. Jaeger, and S. R. Nagel, Density relaxation in a vibrated granular material, *Phys. Rev. E* **51**, 3957 (1995).
- [11] G. Lumay and N. Vandewalle, Experimental study of granular compaction dynamics at different scales: Grain mobility, hexagonal domains, and packing fraction, *Phys. Rev. Lett.* **95**, 028002 (2005).
- [12] P. Philippe and D. Bideau, Compaction dynamics of a granular medium under vertical tapping, *Europhys. Lett.* **60**, 677 (2002).
- [13] G. Lumay and N. Vandewalle, Experimental study of the compaction dynamics for two-dimensional anisotropic granular materials, *Phys. Rev. E* **74**, 021301 (2006).
- [14] N. Mueggenburg, Granular compaction under confinement, *Phys. Rev. E* **85**, 041305 (2012).
- [15] R. Hu, M. Yeung, C. Lee, and S. Wang, Mechanical behavior and microstructural variation of loess under dynamic compaction, *Eng. Geol.* **59**, 203 (2001).
- [16] O. Ben-Nun and I. Einav, The role of self-organization during confined comminution of granular materials, *Philos. Trans. R. Soc. A* **368**, 231 (2010).
- [17] M. M. Bandi, M. K. Rivera, F. Krzakala, and R. E. Ecke, Fragility and hysteretic creep in frictional granular jamming, *Phys. Rev. E* **87**, 042205 (2013).
- [18] J. Ren, J. A. Dijksman, and R. P. Behringer, Reynolds pressure and relaxation in a sheared granular system, *Phys. Rev. Lett.* **110**, 018302 (2013).
- [19] M. Bandi, H. G. E. Hentschel, I. Procaccia, S. Roy, and J. Zylberg, Training, memory and universal scaling in amorphous frictional granular matter, *Europhys. Lett.* **122**, 38003 (2018).
- [20] A. Ghosh, J. Radhakrishnan, P. M. Chaikin, D. Levine, and S. Ghosh, Coupled dynamical phase transitions in driven disk packings, *Phys. Rev. Lett.* **129**, 188002 (2022).
- [21] N. Xu, J. Blawdziewicz, and C. S. O'Hern, Random close packing revisited: Ways to pack frictionless disks, *Phys. Rev. E* **71**, 061306 (2005).
- [22] L. E. Silbert, Jamming of frictional spheres and random loose packing, *Soft Matter* **6**, 2918 (2010).
- [23] J. R. Macdonald and J. C. Phillips, Topological derivation of shape exponents for stretched exponential relaxation, *J. Chem. Phys.* **122**, 074510 (2005).
- [24] M. Potuzak, R. C. Welch, and J. C. Mauro, Topological origin of stretched exponential relaxation in glass, *J. Chem. Phys.* **135**, 214502 (2011).
- [25] Y. Yu, M. Wang, D. Zhang, B. Wang, G. Sant, and M. Bauchy, Stretched exponential relaxation of glasses at low temperature, *Phys. Rev. Lett.* **115**, 165901 (2015).
- [26] J. Phillips, Microscopic aspects of stretched exponential relaxation (SER) in homogeneous molecular and network glasses and polymers, *J. Non-Cryst. Solids* **357**, 3853 (2011).
- [27] H. Tong, P. Tan, and N. Xu, From crystals to disordered crystals: A hidden order-disorder transition, *Sci. Rep.* **5**, 15378 (2015).
- [28] H. Mizuno, S. Mossa, and J.-L. Barrat, Elastic heterogeneity, vibrational states, and thermal conductivity across an amorphisation transition, *Europhys. Lett.* **104**, 56001 (2013).
- [29] T. Bauer, P. Lunkenheimer, and A. Loidl, Cooperativity and the freezing of molecular motion at the glass transition, *Phys. Rev. Lett.* **111**, 225702 (2013).
- [30] A. W. Fitzgibbon, R. B. Fisher *et al.*, A Buyer's Guide to Conic Fitting, in *Proceedings of the 6th British Conference on Machine Vision* (BMVA Press, 1996), Vol. 2, pp. 513–522.
- [31] See Supplemental Material at <http://link.aps.org/supplemental/10.1103/PhysRevResearch.6.033255> for the movies that show the in-plane (S1.mov) and out of plane buckling (S2.mov) behavior.